JOURNAL PRE-PROOF

This is an early version of the article, published prior to copyediting, typesetting, and editorial correction. The manuscript has been accepted for publication and is now available online to ensure early dissemination, author visibility, and citation tracking prior to the formal issue publication.

It has not undergone final language verification, formatting, or technical editing by the journal's editorial team. Content is subject to change in the final Version of Record.

To differentiate this version, it is marked as "PRE-PROOF PUBLICATION" and should be cited with the provided DOI. A visible watermark on each page indicates its preliminary status.

The final version will appear in a regular issue of *Archives of Acoustics*, with final metadata, layout, and pagination.

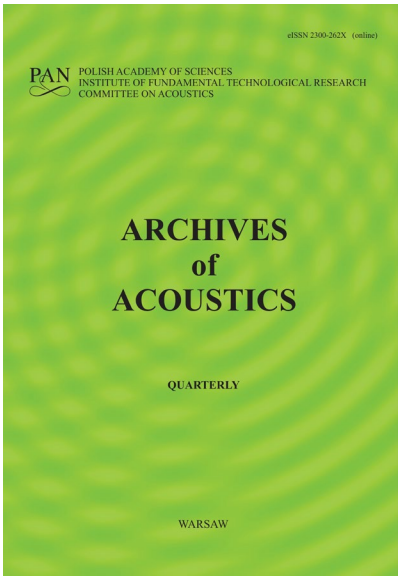

Title: Modeling and investigation of a multi-resonant metamaterial sound insulator

Author(s): Zacharie Laly, Raymond Panneton, Noureddine Atalla, Sebastian Ghinet

DOI: https://doi.org/10.24423/archacoust.2026.4353

Journal: *Archives of Acoustics*

ISSN: 0137-5075, e-ISSN: 2300-262X

Publication status: In press

Received: 2025-10-08

Revised: 2026-04-11

Accepted: 2026-04-15

Published pre-proof: 2026-04-27

Please cite this article as:

Laly Z., Panneton R., Atalla N., Ghinet S. (2026), Modeling and investigation of a multi-resonant metamaterial sound insulator, *Archives of Acoustics*, https://doi.org/10.24423/archacoust.2026.4353

Modeling and investigation of a multi-resonant metamaterial sound insulator

Zacharie LALY[a,*], Raymond PANNETON[a], Noureddine ATALLA[a], Sebastian GHINET[b]

[a] *Centre de Recherche Acoustique–Signal–Humain de l'Université de Sherbrooke (CRASH-UdeS), 2500 Boul. de l'université, J1K 2R1, Sherbrooke, Québec, Canada*

[b] *National Research Council Canada, Aerospace, Ottawa, ON K1A 0R6, Canada*

Abstract

A design of multi-resonant acoustic metamaterial sound insulator is proposed to attenuate multi-tonal and broadband noise. The unit cell of the metamaterial consists of a porous material with four, nine, and sixteen embedded Helmholtz resonators and its sound attenuation performance is studied using finite element method (FEM). A theoretical approach based on transfer matrix method is proposed and the theoretical results of the sound absorption and the transmission loss (TL) agree well with FEM results. Compared to the porous layer with one embedded resonator that presents one TL and one sound absorption resonant peak, the metamaterial made of four, nine, and sixteen embedded resonators exhibits respectively four, nine and sixteen sound absorption and TL resonant peaks. The sound absorption at various incidence angles and the diffuse field sound absorption of the proposed metamaterial are studied. At each resonant frequency, the acoustic pressure is maximum in the cavity of the corresponding resonator while in the associated neck, the acoustic velocity is maximum with important acoustic power dissipation density. As the incidence angle increases, the acoustic pressure in the cavity at the resonant frequencies decreases as well as the velocity in the necks and the power dissipation density becomes negligible, resulting in a decrease of the sound absorption. As the number of resonators within the porous layer increases, the sound absorption and TL frequency band enlarges. Compared to the conventional porous layer, the sound absorption and the TL are significantly improved at the resonant frequencies of the resonators.

Keywords: porous material, Helmholtz resonators, sound absorption, transmission loss, acoustic metamaterial.

1. Introduction

* Corresponding author.
E-mail address: Zacharie.Laly@usherbrooke.ca (Z. Laly)

Porous materials are widely used for noise reduction in many applications such as construction, transport, and manufacturing. Their microstructure featuring high porosity, a complex and interconnected pore network, and a large internal surface area allows the sound waves to enter the media that dissipates their energy by viscous and thermal losses (Allard and Atalla, 2009). Porous materials are inefficient at low frequencies while they provide efficient sound dissipation at high frequencies. This limitation can be overcome by the use of inner inclusions within the porous layer. Boutin and Becot (Boutin and Becot, 2015) reported theoretical and experimental analysis on the acoustics of gas saturated rigid porous media with inner resonators. They observed that the resonators modify the effective bulk modulus of the medium which induces strong velocity dispersion and high attenuation around the resonance frequencies. They tested experimentally several prototypes of such media and compared the measurement with the theory. The sound attenuation performance of a cellular porous material with resonant inclusions was investigated by Doutres et al. (Doutres, Atalla and Osman, 2015). Using theoretical, numerical and experimental approaches, they demonstrated the transmission loss (TL) improvement of the material at the resonance frequency of the embedded Helmholtz resonator (HR). They illustrate that the impact of the resonator on the material's sound absorption performance can be positive or negative. Lagarrigue et al. (Lagarrigue *et al.*, 2013) studied the sound attenuation performance of porous material with arranged resonant inclusions (slotted cylinders) that are periodically embedded into the porous matrix and they observed the sound absorption improvement. Zhu et al. (Zhu *et al.,* 2019) proposed a sound absorber composed of a porous layer embedded with periodic resonators made of two 180° twisted split rings. They demonstrated that a single resonator embedded in the porous material can achieve perfect absorption at its resonance frequency, which can be tuned by adjusting the resonator's inner radius. When four twisted split rings were incorporated into the porous layer, the sound absorption coefficient was improved. Abbad et al. (Abbad *et al.,* 2019) studied a front membrane-cavity Helmholtz resonator embedded within a porous material and showed the transmission loss enhancement at the Helmholtz resonance. However, they found that the presence of the resonator can reduce the overall sound absorption performance, depending on the membrane's resonance frequency and they recommended the transmission configuration for application of the proposed design. Ghinet et al.(Ghinet et al., 2020) studied the single and double wall configurations of glass wool layers with embedded periodic Helmholtz resonators for aircraft cabin applications. The TL of the studied design was experimentally evaluated under diffuse field

excitation. Kone et al. (Kone *et al.*, 2021, 2022) investigated glass wool with embedded resonator having complex neck shape for aircraft cabin applications and they illustrated multiple sound absorption peaks. Magliacano et al. (Magliacano *et al.*, 2024) used finite element method (FEM) and transfer matrix method (TMM) to investigate the sound attenuation characteristics of porous material with embedded periodic pattern such as hollow cylindrical inclusions, half-cut hollow cylindrical inclusions and Helmholtz resonators. The FEM results were compared with experiments. Helmholtz resonators with porous material lining was modeled by Zhang and Xin (Zhang and Xin, 2024) using the double porosity method. They demonstrated that the porous lining, as an additional damping helps to satisfy the impedance matching condition leading to the sound absorption improvement compared to the classic HR. Laly et al. (Laly, Panneton and Atalla, 2022; Laly *et al.*, 2023; Laly, Mechefske, Ghinet and Kone, 2024) proposed transfer matrix methods to model acoustic metamaterial consisting of porous materials with embedded periodic Helmholtz resonators. The results of the TMM were validated by comparison with FEM in single and double wall configurations. They demonstrated the impacts of the parameters of the periodic resonator on the TL and studied the influences of the elasticity of the resonator's walls on the sound attenuation performance (Laly, Mechefske, Ghinet, Kone, *et al.*, 2024). Porous material with conventional embedded Helmholtz resonator provides only one resonant peak with narrow frequency band.

In this paper, a multi-resonant acoustic metamaterial based on porous material with multiple embedded Helmholtz resonators is presented for multi-tonal and broadband noise reduction. The theoretical model using transfer matrix method shows good agreement with finite element method. The transmission loss and the diffuse field sound absorption of the metamaterial are significantly improved at the resonant frequencies of the resonators with the frequency band that increases as the number of resonators within the unit cell increases. The sound attenuation mechanism of the metamaterial is studied. The paper is organized as follows. In section 2, the design of the proposed metamaterial is presented and section 3 shows the theoretical modelling. The comparison of the theory with finite element method is shown in section 4 and the analysis of the sound attenuation performance is performed in section 5 and finally the conclusion is presented in section 6.

2. Finite element modeling of multi-resonant acoustic metamaterial

Low-frequency noise poses challenges in many engineering applications due to its long wavelength, which makes conventional porous materials ineffective. In this paper, an acoustic

metamaterial design consisting of multiple resonators periodically embedded within a porous material is proposed to effectively control multi-tonal low-frequency noise. Figure 1 presents the unit cell of the proposed metamaterial that consists of a porous material with embedded multiple Helmholtz resonators. In Fig. 1(b), four different resonators are integrated within the porous material and Fig. 1(c) illustrates the porous layer with nine different embedded resonators. In Fig. 1(d), sixteen different Helmholtz resonators are embedded within the porous layer and in Fig. 1(a), the porous layer with one embedded resonator is shown for comparison. The cavities of the resonators have cylindrical shapes as well as the necks that are extended into the cavities. In Fig. 1, all the resonators have identical cavities with diameter of 40 mm and in Fig. 1 (b), (c) and (d), the necks of the resonators have different geometric parameters illustrated by different colors while the cavities are separated from each other by an equal distance. The distance between the cavities axes of two adjacent resonators is 60 mm. In Fig. 1(c), the nine cavities are identical and the geometric parameters of the nine necks are different, illustrated by different colors. Similarly, the sixteen cavities in Fig. 1(d) are identical with sixteen necks having different geometric parameters. The walls of the necks and the cavities in Fig. 1 are considered rigid and the thickness of the porous material is equal to the length of each resonator. The resonators are arranged in parallel within the porous material.

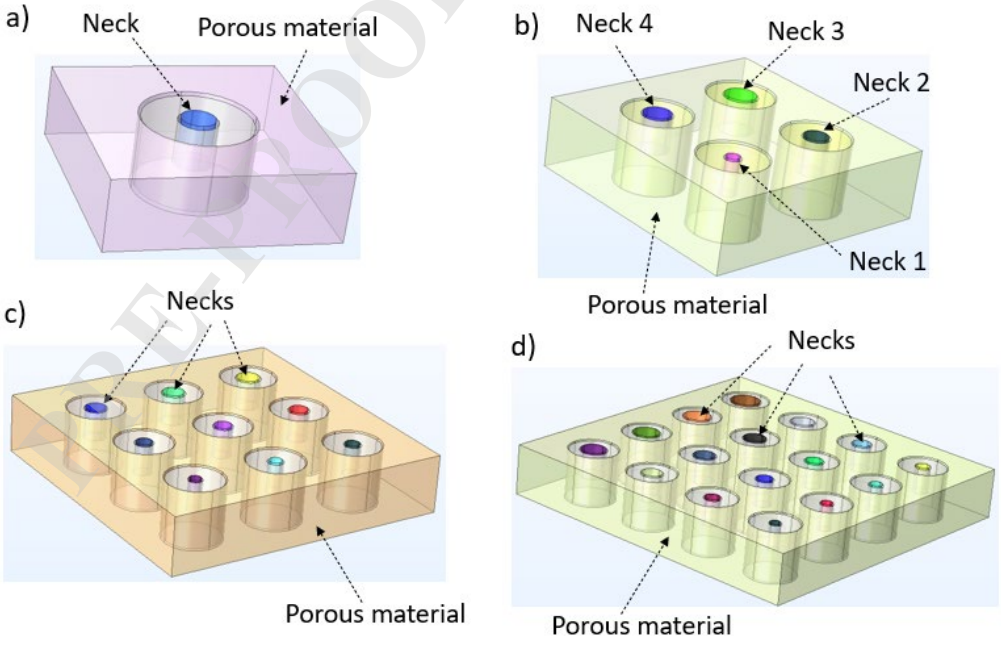

Fig. 1. Acoustic metamaterial based on porous layer with embedded multiple resonators: (a) one periodic resonator, (b) four periodic resonators (c) nine periodic resonators (d) sixteen periodic resonators.

The sound attenuation performances of the metamaterial in Fig. 1 are studied numerically using COMSOL Multiphysics and the simulations are conducted with one periodic unit cell (PUC). Figure 2 shows the numerical models of the PUC for the transmission loss calculations. The PUC is made of an incident fluid, a transmission fluid and the porous layer with multiple embedded resonators. The incident and transmission fluids have identical length.

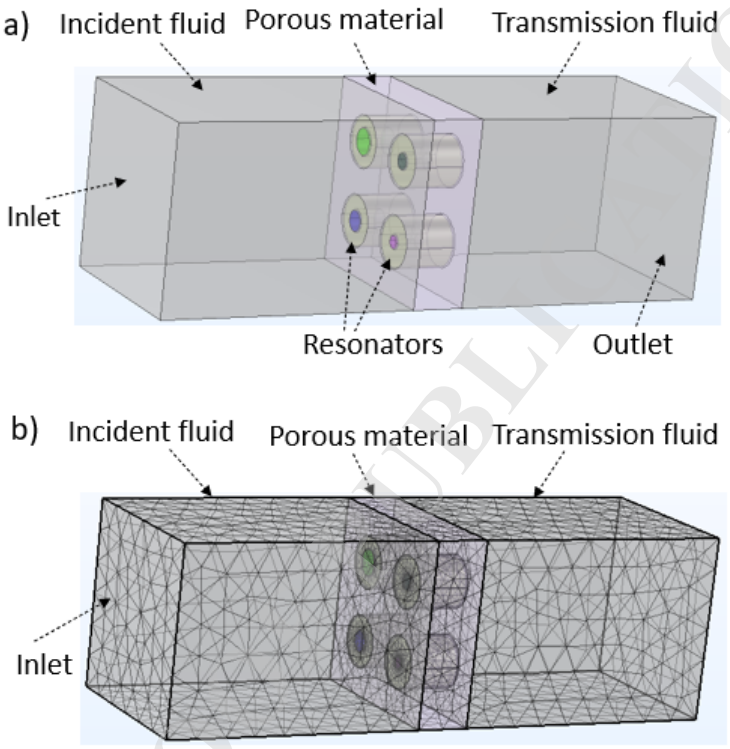

Fig. 2. PUC of the metamaterial (a) geometry with four HR, (b) mesh with four HR.

A normal incidence plane wave with pressure amplitude of 1 Pa is imposed on the inlet plane in Fig. 2 and plane wave radiation condition is applied on the inlet and outlet planes while periodic boundary conditions are applied on all parallel planes in Fig. 2. The transmission loss is given by

$$TL = 10\log_{10}\left(\frac{W_i}{W_t}\right) \tag{1}$$

where W_t and W_i are the transmitted and incident sound power at the outlet and inlet planes respectively.

Figure 3 presents the finite element models of the PUC for studying the diffuse field sound absorption performance of the metamaterial. The PUC in Fig. 3 consists of a perfectly matched layer (PML); a background acoustic pressure field and the porous material with embedded multiple

resonators. Figure 3(a), (b), (c) and (d) show respectively the PUC with one, four, nine and sixteen resonators. The background pressure field provides an incident plane wave in the z direction with an amplitude of 1 Pa, an incident angle θ, and an azimuthal angle ψ. The PML creates a virtual anechoic incident domain to eliminate the reflection of acoustic waves from the metamaterials.

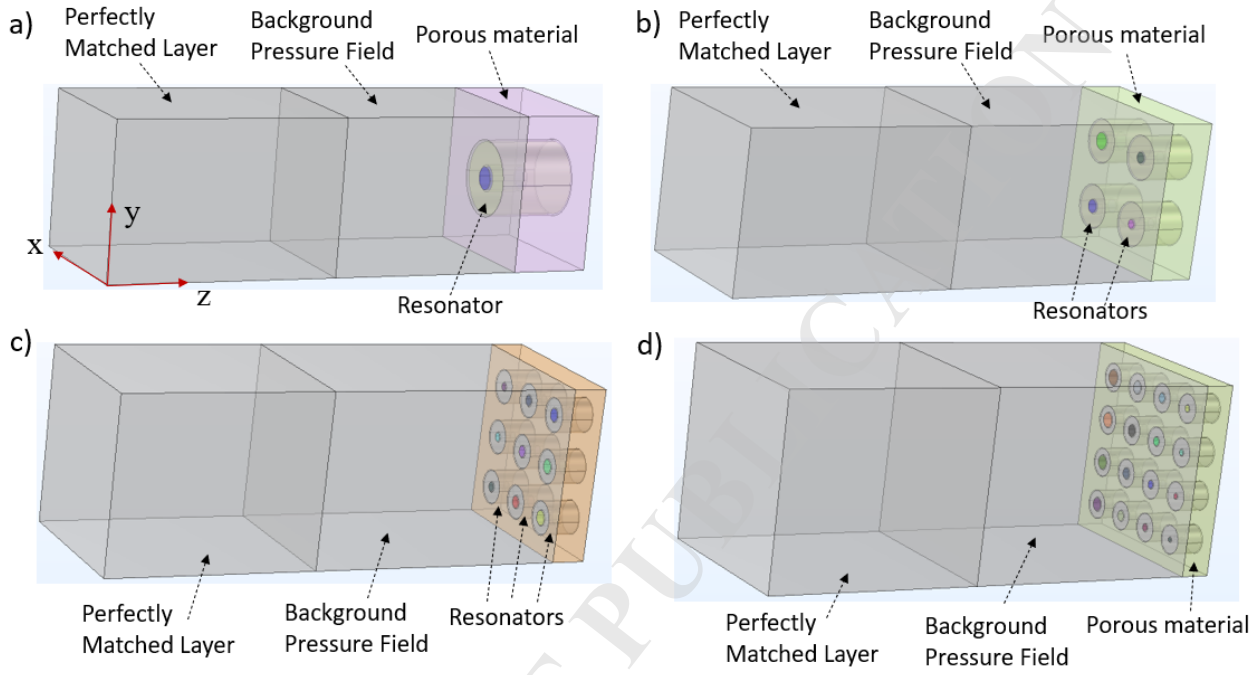

Fig. 3. PUC of the metamaterial for sound absorption estimation: (a) PUC with 1 HR, (b) PUC with 4 HR, (c) PUC with nine HR (d) PUC with sixteen HR.

The porous material as well as the air inside the neck of each resonator in Figs. 2 and 3 are modeled using the equivalent fluid model of Johnson-Champoux-Allard with the equivalent density $\rho_{eq}(\omega)$ and bulk modulus $K_{eq}(\omega)$ given by (Allard and Atalla, 2009)

$$\rho_{eq}(\omega) = \alpha_\infty \rho_0 \left(1 + \frac{\sigma\phi}{j\omega\alpha_\infty\rho_0} \sqrt{1 + \frac{4j\rho_0\omega\eta\alpha_\infty^2}{\phi^2\sigma^2\Lambda^2}} \right), \tag{2}$$

$$K_{eq}(\omega) = \gamma P_0 \left[\gamma - \frac{\gamma - 1}{1 + \frac{8\eta}{j\omega\rho_0 P_r \Lambda'^2} \sqrt{1 + \frac{j\omega\rho_0 P_r \Lambda'^2}{16\eta}}} \right]^{-1}, \tag{3}$$

with ϕ the porosity, σ the static airflow resistivity, α_∞ the tortuosity, ρ_0 is the density , Λ the viscous characteristic length, Λ' the thermal characteristic length, η is the dynamic viscosity, P_r

the Prandtl number, γ is the specific heat ratio, and P_0 is the atmospheric static pressure. The tortuosity and the porosity of the air inside each neck are set to 1. The static airflow resistivity of the i^{th} neck is given by $\sigma_i = \dfrac{8\eta}{\phi_i R_i^2}$ with ϕ_i the porosity of the air inside the i^{th} neck and R_i the radius of the i^{th} neck whose viscous characteristic length is equal to R_i. The rest of the domains in Figs. 2 and 3 are characterized using the pressure acoustics module of COMSOL.

The oblique incident acoustic plane wave reaching the surface of the porous layer with embedded resonators is given by

$$P_i(\theta,\psi) = P_A e^{-j\left(k_x x + k_y y + k_z z\right)} \tag{4}$$

with $P_A = 1$ Pa and j the imaginary unit ($j^2 = -1$). The acoustic wavenumbers k_x, k_y and k_z in Eq. (4) are given by

$$\begin{cases} k_x = k_0 \sin\theta\cos\psi \\ k_y = k_0 \sin\theta\sin\psi \\ k_z = k_0 \cos\theta \end{cases} \tag{5}$$

with $k_0 = \omega/c_0$, where ω is the angular frequency and c_0 the speed of sound in air. Floquet periodic boundary conditions are imposed on all opposing parallel boundaries of the geometry in Fig. 3. The k wave vector for Floquet periodicity is given by k = [k_x k_y 0]. The surface average of the total acoustic pressure P_t at the inlet surface of the metamaterial in Fig. 3 is determined numerically and the complex reflection coefficient is then obtained by

$$R(\theta,\psi) = \frac{P_t(\theta,\psi) - P_i(\theta,\psi)}{P_i(\theta,\psi)}. \tag{6}$$

The normalized surface acoustic impedance $Z_s(\theta,\psi)$ and the sound absorption coefficient $\alpha(\theta,\psi)$ of the metamaterial for each incidence angle θ are expressed by

$$Z_s(\theta,\psi) = \frac{1+R(\theta,\psi)}{\left(1-R(\theta,\psi)\right)\cos(\theta,\psi)}, \quad \alpha(\theta,\psi) = 1 - \left|R(\theta,\psi)\right|^2 \tag{7}$$

The diffuse field sound absorption coefficient for different incident waves with an incidence angle θ varying between 0 and θ_{max}, where θ_{max} is the maximum incidence angle is then determined by (LALY *et al.*, 2025)

$$\alpha_D = \frac{\int_0^{\theta_{\max}} \alpha(\theta)\sin(2\theta)\,d\theta}{\int_0^{\theta_{\max}} \sin(2\theta)\,d\theta}. \quad (8)$$

A discretized form of this equation is used in the numerical calculations with $\theta_{\max}$ set to $\pi/2$ and the azimuthal angle ψ set to zero.

The thickness of the porous layer is set to 40 mm which is equal to the length of the cavity of each resonator. The static airflow resistivity of the porous layer is 26000 N s m^{-4} with open porosity of 99%, a tortuosity of 1.02 and the viscous and thermal characteristic lengths are respectively 150 μm and 300 μm. With one resonator within the porous material as shown in Fig. 3(a), the radius of the neck is set to 4 mm with a length of 20 mm and the lateral dimensions of the PUC are set to 80 mm x 80 mm. For the metamaterial with four resonators embedded within the porous layer, the radii of the four necks are 4.5 mm, 5 mm, 5.5 mm, and 6 mm respectively with an identical length of 20 mm. In Fig. 3(c) where nine resonators are embedded within the porous layer, the radii of the nine resonators are respectively 4.5 mm, 5 mm, 5.5 mm, 6 mm, 6.5 mm, 7 mm, 7.5 mm, 8 mm and 8.5 mm with a same length of 20 mm and the lateral dimensions of the PUC are 200 mm x 200 mm. In Fig. 3(d), the length of the sixteen different necks of the resonators is equal to 20 mm and the radii are varied between 3 mm and 10.5 mm with a step of 0.5 mm.

3. Theoretical modeling

In this section, a theoretical approach is presented to model the porous material with embedded multiple resonators. Figure 4 shows the porous material with four embedded resonators having different necks illustrated by different colors. The periodic unit cell is divided into four regions denoted by layer 1 to layer 4 where the lateral dimensions of each sub-porous layer *i* (*i = 1,2,3,4*) are 70 mm x 70 mm and that of the unit cell are 140 mm x 140 mm. Layer *i* is made of the sub-porous layer *i* with the embedded resonator *i*.

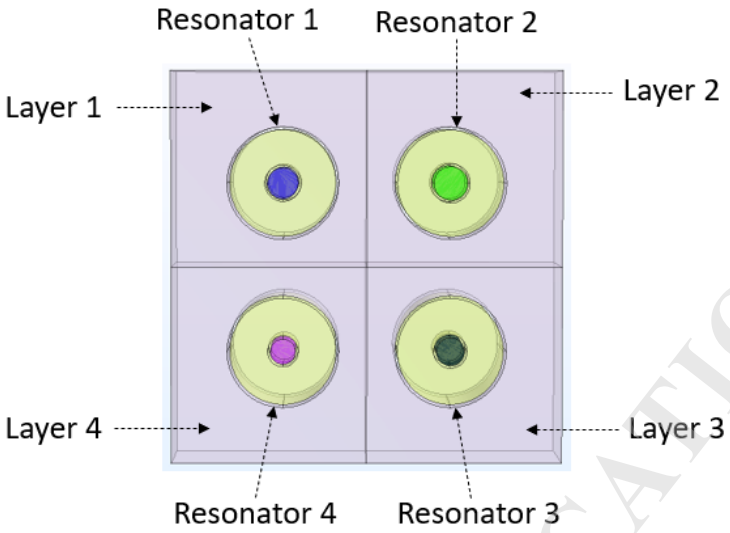

Fig. 4. Porous material with four embedded resonators.

The following assumptions are assumed: (1) normal incidence plane wave propagation, (2) there is no pressure diffusion between adjacent parallel elements, (3) the wavelength is much larger than the PUC and (4) each element namely the porous layer and each resonator can be modeled by a 2x2 transfer matrix. The acoustic impedance of the Helmholtz resonator alone without the porous layer can be expressed as (Doutres, Atalla and Osman, 2015; Laly *et al.*, 2023)

$$Z_H^i = \frac{1}{s_e^i}\left(Z_{neck}^i - j s_v^i Z_0 \cot(kL_c^i)\right) \tag{9}$$

where Z_0 is the characteristic impedance of air, Z_{neck}^i is the impedance of the i^{th} neck, L_c^i is the i^{th} resonator cavity thickness, s_e^i and s_v^i represent respectively the ratio of the i^{th} neck aperture surface over the cross-section area of i^{th} external elementary cell and internal elementary cell. The acoustic impedance of the i^{th} neck is given by (Doutres, Atalla and Osman, 2015; Laly, Mechefske, Ghinet and Kone, 2024)

$$Z_{neck}^i = R_s\left(4 + \frac{2H_i}{R_i}\right) + j\omega\rho_0\left(\delta_i + \varepsilon_i + H_i\right), \tag{10}$$

where R_i and H_i are the radius and the length of the i^{th} neck, δ_i and ε_i are the correction lengths and R_s is a surface resistance that is given by $R_s = 0.5\sqrt{2\eta\rho_0\omega}$. Since each resonator neck is circular, the approximation of the two corrections lengths for $s_e^i < 0.16$ is

$$\delta_i = \varepsilon_i = 0.48\sqrt{S_n^i}\left(1-1.14\sqrt{s_e^i}\right), \tag{11}$$

where S_n^i is the neck surface of the i^{th} resonator. The transfer matrix T_H^i of the i^{th} resonator can be written as

$$T_H^i = \begin{bmatrix} 1 & 0 \\ 1/Z_H^i & 1 \end{bmatrix}\begin{bmatrix} 1 & j\omega M_s^i \\ 0 & 1 \end{bmatrix} = \begin{bmatrix} T_{H11}^i & T_{H12}^i \\ T_{H21}^i & T_{H22}^i \end{bmatrix} \tag{12}$$

with M_s^i the mass per unit area of the i^{th} resonator ($M_s^i = \rho_0\left(\delta_i + \varepsilon_i + H_i\right)$). From Eq. (12), the admittance matrix Y_H^i of the i^{th} resonator can be obtained (Verdière *et al.*, 2013)

$$Y_H^i = \frac{1}{T_{H12}^i}\begin{bmatrix} T_{H22}^i & T_{H21}^i T_{H12}^i - T_{H22}^i T_{H11}^i \\ 1 & -T_{H11}^i \end{bmatrix}. \tag{13}$$

The transfer matrix T_p^i of each layer *i* of the porous material in Fig. 4 is determined using the equivalent density $\rho_{eq}(\omega)$ and bulk modulus $K_{eq}(\omega)$ given by Eqs. (2) and (3). It is expressed by

$$T_P^i = \begin{bmatrix} \cos\left(k_{eq}^i L_i\right) & jZ_{eq}^i \sin\left(k_{eq}^i L_i\right) \\ j\dfrac{\sin\left(k_{eq}^i L_i\right)}{Z_{eq}^i} & \cos\left(k_{eq}^i L_i\right) \end{bmatrix} = \begin{bmatrix} T_{P11}^i & T_{P12}^i \\ T_{P21}^i & T_{P22}^i \end{bmatrix} \tag{14}$$

where L_i is the thickness of the i^{th} layer, Z_{eq}^i and k_{eq}^i are the characteristic impedance and the wave number of the equivalent fluid of i^{th} layer given by

$$Z_{eq}^i = \sqrt{\rho_{eq}K_{eq}}/\phi \ , \ k_{eq}^i = \omega\sqrt{\rho_{eq}/K_{eq}} \ . \tag{15}$$

From Eq. (15), the admittance matrix Y_p^i of each layer of the porous material in Fig. 4 is obtained. It is given by

$$Y_P^i = \frac{1}{T_{P12}^i}\begin{bmatrix} T_{P22}^i & T_{P21}^i T_{P12}^i - T_{P22}^i T_{P11}^i \\ 1 & -T_{P11}^i \end{bmatrix}. \tag{16}$$

Each ith layer of porous material with the embedded ith resonator in Fig. 4 are assembled in parallel, so their equivalent transfer matrix M^i is determined using the parallel transfer matrix method (Verdière *et al.*, 2013)

$$M^i = \frac{-1}{\sum r_n^i Y_{n21}^i}\begin{bmatrix} \sum r_n^i Y_{n22}^i & -1 \\ \sum r_n^i Y_{n22}^i \sum r_n^i Y_{n11}^i - \sum r_n^i Y_{n12}^i \sum r_n^i Y_{n21}^i & -\sum r_n^i Y_{n11}^i \end{bmatrix}. \tag{17}$$

where, Y_n^i represent the admittance matrix components of Eqs. (13) and (16) with $n = H$ for the resonator and $n = P$ for the porous substrate and r_n^i is the surface ratio of each element given by

$$r_H^i = S_i / S_P^i, \quad r_P^i = 1 - r_H^i, \tag{18}$$

with S_P^i the surface of the i^{th} unit cell layer and S_i the surface of the i^{th} resonator. The transfer matrices of Layer 1, Layer 2, Layer 3 and Layer 4 in Fig. 4 are then respectively denoted by M^1, M^2, M^3 and M^4. Thus, the admittance matrix of each i[th] layer in Fig. 4 is obtained from Eq. (17) and is expressed by

$$Y^i = \frac{1}{M_{12}^i}\begin{bmatrix} M_{22}^i & M_{21}^i M_{12}^i - M_{22}^i M_{11}^i \\ 1 & -M_{11}^i \end{bmatrix} \tag{19}$$

In Fig. 4, Layer 1 and Layer 2 are assembled in parallel, thus the equivalent transfer matrix TM^a of Layer 1 and Layer 2 is determined by

$$TM^a = \frac{-1}{\sum r_m Y_{21}^m}\begin{bmatrix} \sum r_m Y_{22}^m & -1 \\ \sum r_m Y_{22}^m \sum r_m Y_{11}^m - \sum r_m Y_{12}^m \sum r_m Y_{21}^m & -\sum r_m Y_{11}^m \end{bmatrix} \tag{20}$$

In Eq. (20), *m=1,2*, Y^m is obtained from Eq. (19), $r_1 = S_1^L / S_{12}^L$, $r_2 = 1 - r_1$ with S_1^L the surface of Layer 1 and S_{12}^L the surface of both Layer 1 and Layer 2.

Similarly, Layer 3 and Layer 4 in Fig. 4 are assembled in parallel, so their equivalent transfer matrix TM^b is given by

$$TM^b = \frac{-1}{\sum r_u Y_{21}^u}\begin{bmatrix} \sum r_u Y_{22}^u & -1 \\ \sum r_u Y_{22}^u \sum r_u Y_{11}^u - \sum r_u Y_{12}^u \sum r_u Y_{21}^u & -\sum r_u Y_{11}^u \end{bmatrix} \tag{21}$$

where *u=3,4*, Y^u is given by Eq. (19), $r_3 = S_3^L / S_{34}^L$, $r_4 = 1 - r_3$ with S_3^L the surface of Layer 3 and S_{34}^L the surface of both Layer 3 and Layer 4. If the parallel assembly of Layer 1 and Layer 2 is denoted by material A and the parallel assembly of Layer 3 and Layer 4 by material B, then material A and B are arranged in parallel and their admittance matrices can be expressed as

$$YM^q = \frac{1}{TM_{12}^q}\begin{bmatrix} TM_{22}^q & TM_{21}^q TM_{12}^q - TM_{22}^q TM_{11}^q \\ 1 & -TM_{11}^q \end{bmatrix} \tag{22}$$

In Eq. (22), $q = a, b$ and TM^q is obtained from Eqs. (20) and (21). The transfer matrix of the porous material with four embedded Helmholtz resonators in Fig. 4 is finally determined by

$$TG = \frac{-1}{\sum r_q YM_{21}^q}\begin{bmatrix} \sum r_q YM_{22}^q & -1 \\ \sum r_q YM_{22}^q \sum r_q YM_{11}^q - \sum r_q YM_{12}^q \sum r_q YM_{21}^q & -\sum r_q YM_{11}^q \end{bmatrix} \tag{23}$$

The transfer matrix in Eq. (23) can be expressed as $TG = \begin{bmatrix} TG_{11} & TG_{12} \\ TG_{21} & TG_{22} \end{bmatrix}$. The theoretical sound absorption coefficient α_{theo} of the metamaterial in Fig. 4 can be calculated using the components of the matrix TG

$$\alpha_{theo} = 1 - \left| \frac{TG_{11} - Z_0 TG_{21}}{TG_{11} + Z_0 TG_{21}} \right|^2 \tag{24}$$

The theoretical transmission loss TL_{theo} of the metamaterial consisting of the porous layer with four embedded resonators is obtained from Eq. (23) and is given by

$$TL_{theo} = -20 \log_{10} \left| \frac{2}{TG_{11} + TG_{12} / Z_0 + Z_0 TG_{21} + TG_{22}} \right| \tag{25}$$

4. Comparison of finite element method and the theory

In this section, the sound absorption coefficient and the TL predicted theoretically using Eqs. (24) and (25) are compared with the results of the finite element method. Figure 5 presents the comparison of the sound absorption coefficient of the metamaterial of Fig. 1(a) made of porous material with one embedded periodic resonator and the comparison of the corresponding TL is shown in Fig. 6. The absorption coefficient of the material with one embedded resonator presents a peak of 0.9 at 364 Hz while without the resonator the absorption coefficient value is 0.34 at 364 Hz. The theoretical calculation agrees well with FEM. In Fig. 6, the FEM result of the TL with the resonator shows a peak of 18 dB at 364 Hz and the theoretical TL peak at this frequency is 17 dB. Without the resonator, the TL of the porous material alone is lower than 8 dB over the entire frequency range.

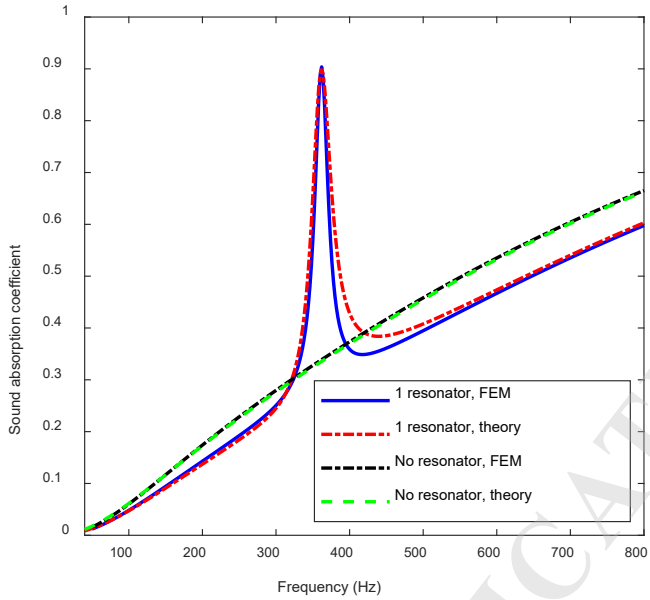

Fig. 5. Comparison of the sound absorption coefficient of the metamaterial with one embedded resonator.

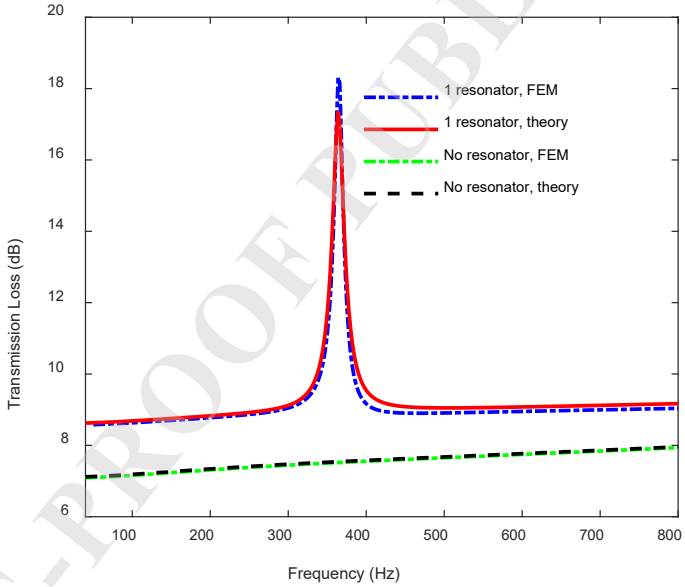

Fig. 6. Comparison of the transmission loss of the metamaterial with one embedded resonator.

Figure 7 presents the comparison of the theoretical absorption coefficient and FEM result for the metamaterial of Fig. 1(b) consisting of the porous layer with four embedded different resonators and the comparison of the corresponding TL is shown in Fig. 8. The absorption coefficient as well as the TL exhibit four resonance peaks at 408 Hz, 448 Hz, 490 Hz and 530 Hz. The FEM peak values of the sound absorption are 0.98, 0.99, 0.98 and 0.92 respectively while the theoretical values are 0.94, 0.99, 0.99 and 0.97. The peaks of the TL predicted by FEM are 13 dB, 14 dB, 15.2 dB and 16 dB respectively and for the theory, the peaks of the TL are 12.7 dB, 13.5 dB, 14 dB and

15 dB. The results of theory and FEM in Figs. 7 and 8 are in good agreement. With four parallel resonators embedded within the porous layer, the sound absorption and the TL present four different resonant peaks while only one resonant peak is observed in Figs. 5 and 6 for one resonator incorporated within the porous material.

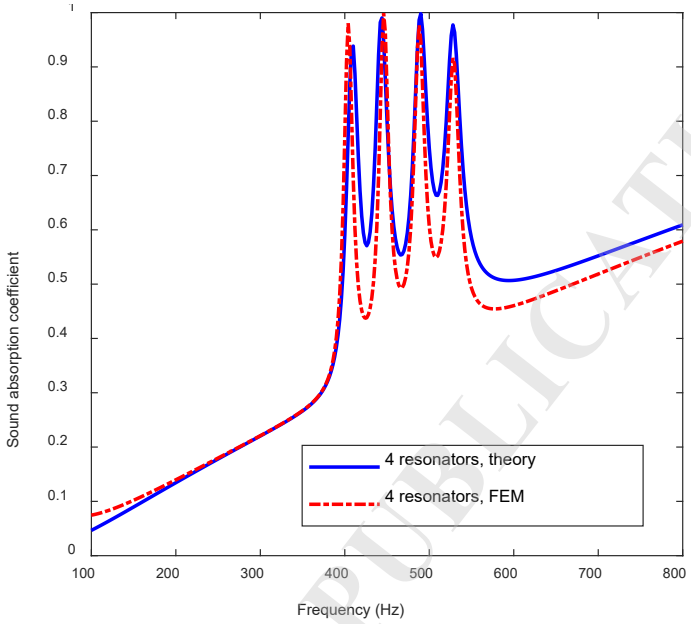

Fig. 7. Comparison of the sound absorption coefficient of the metamaterial with four embedded resonators.

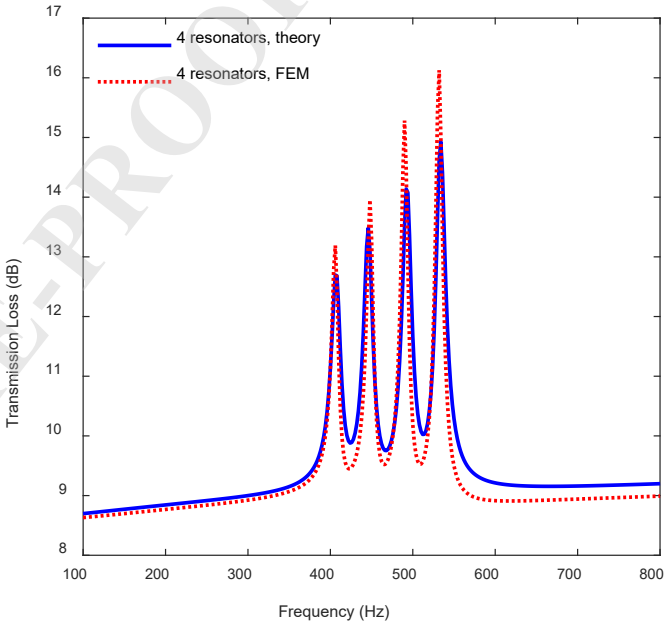

Fig. 8. Comparison of the transmission loss of the metamaterial with four embedded resonators.

For a plane wave impinging on the metamaterial surface with an incidence angle θ, the theoretical sound absorption coefficient and the transmission loss can be determined by (Verdière *et al.*, 2013)

$$\alpha_\theta = 1 - \left| \frac{T_{11}\cos\theta - Z_0 T_{21}}{T_{11}\cos\theta + Z_0 T_{21}} \right|^2 \tag{26}$$

$$TL_\theta = 20\log_{10}\left(\frac{1}{2}\left| \left(T_{11} + \frac{T_{12}\cos\theta}{Z_0} + \frac{Z_0 T_{21}}{\cos\theta} + T_{22} \right) \right| \right). \tag{27}$$

In Eqs. (26) and (27), T_{11}, T_{12}, T_{21} and T_{22} are the components of the global matrix of the metamaterial made of the porous layer with embedded resonators that can be obtained using Eqs. (17) and (23). Figure 9 presents the comparison of the sound absorption coefficient of the porous layer with one and four embedded resonators for an incidence angle of 30°. It can be observed that the oblique incidence sound absorption predicted theoretically agrees with FEM.

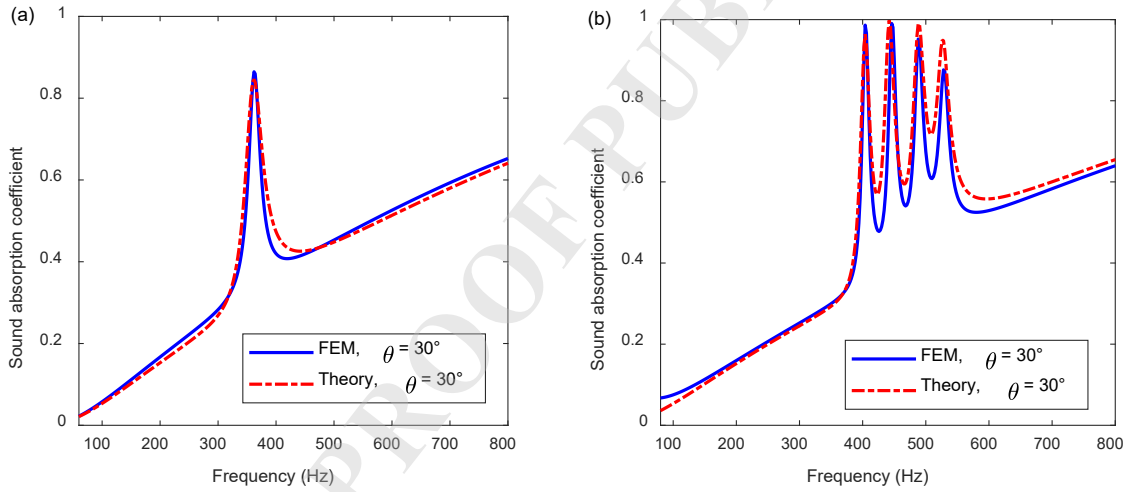

Fig. 9. Sound absorption coefficient for oblique incidence (a) one embedded resonator (b) four embedded resonators.

Figure 10(a) and (b) shows the porous material with four embedded resonators and the distance L separating the axes of two adjacent resonators is varied to analyze the interaction effect between the resonators. Figure 10(c), (d), and (e) illustrates the porous material with one, four, and nine perforations in place of the resonators. The diameter of each perforation is identical to that of the cavity of each resonator, which is 40 mm. The absorption coefficient of the porous material with embedded resonators and with perforations is studied in the following section. In Fig. 10(a) and (b), the lateral dimensions are 200 mm x 200 mm and the distance between the axes of two adjacent

resonators is set to 45 mm in Fig. 10(a), while it is 110 mm in Fig. 10(b). The normal incidence sound absorption coefficient of these two configurations is illustrated in Fig. 11, where configuration A represents the case of L equal to 45 mm. With configuration A, the values of the first and fourth absorption peaks are 0.86 and 0.97, while they are 0.83 and 0.98 respectively for configuration B. A slight difference is also observed for frequencies above 550 Hz that should be caused by the interaction effect between the resonators, which is not considered in the analytical model. The minor deviation observed between the theoretical model and FEM results in Figs. 7 and 8 may also result from coupling effects between the resonators.

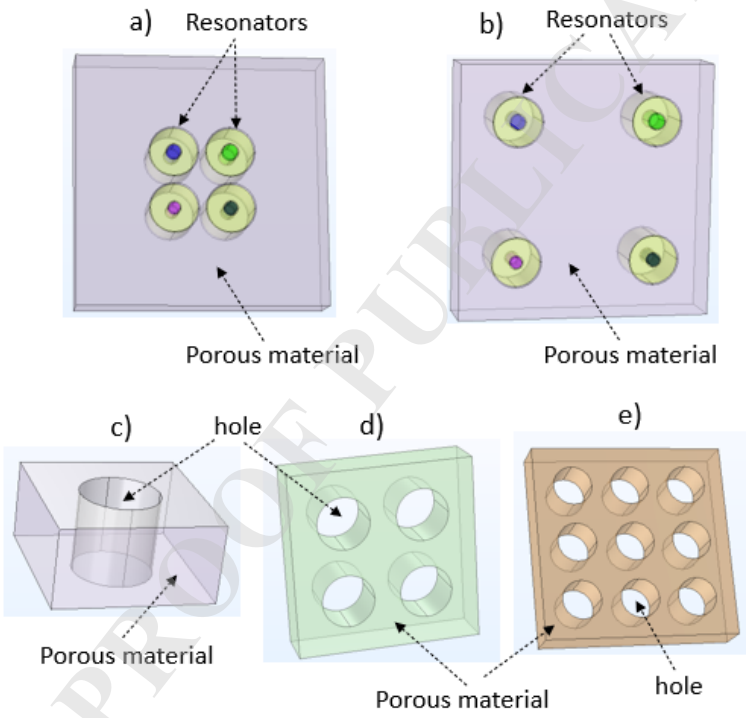

Fig. 10. Geometrical models (a) porous layer with four resonators, L=45 mm (b) porous layer with four resonators, L=110 mm (c) porous layer with one perforation (d) porous layer with four perforations (e) porous layer with nine perforations.

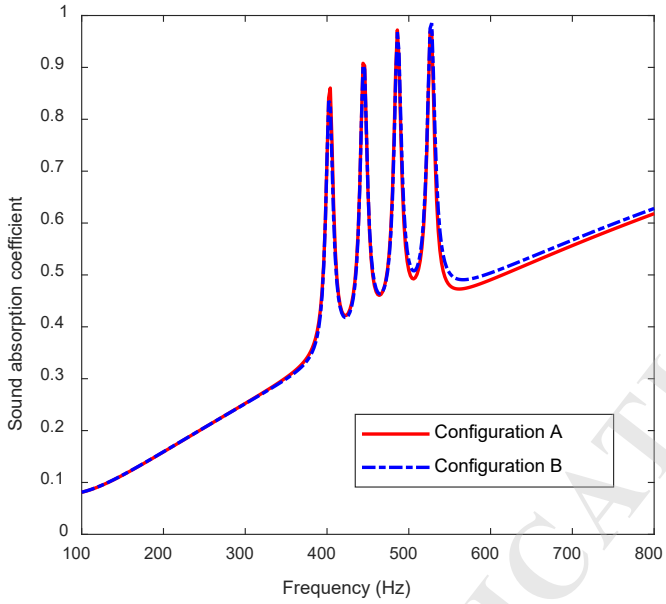

Fig. 11. Sound absorption coefficient.

5. Analysis of the sound attenuation performance

In this section, the sound attenuation performance of the proposed metamaterial is studied numerically. The diffuse field sound absorption coefficient is obtained using Eq. (8) where θ_{max} is set to $\pi/2$.

Figure 12 shows the sound absorption coefficient of the porous layer with one embedded periodic Helmholtz resonator (Fig. 1(a)) at different oblique incidence angles θ. The sound absorption coefficients of the porous layer without resonators and with one and four perforations in the place of resonators as illustrated in Fig. 10(c) and (d) are also presented. The normal incidence sound absorption coefficient in Fig. 12 presents a resonant peak of 0.9 at 362 Hz. For $\theta = 60°$, the absorption coefficient shows a peak of 0.77 at 372 Hz while the diffuse field sound absorption coefficient presents a peak of 0.76 at 364 Hz. The normal incidence sound absorption coefficient of the porous material alone is lower than 0.5 for frequencies below 500 Hz. With one or four perforations within the porous layer, the sound absorption is lower than that of porous layer alone.

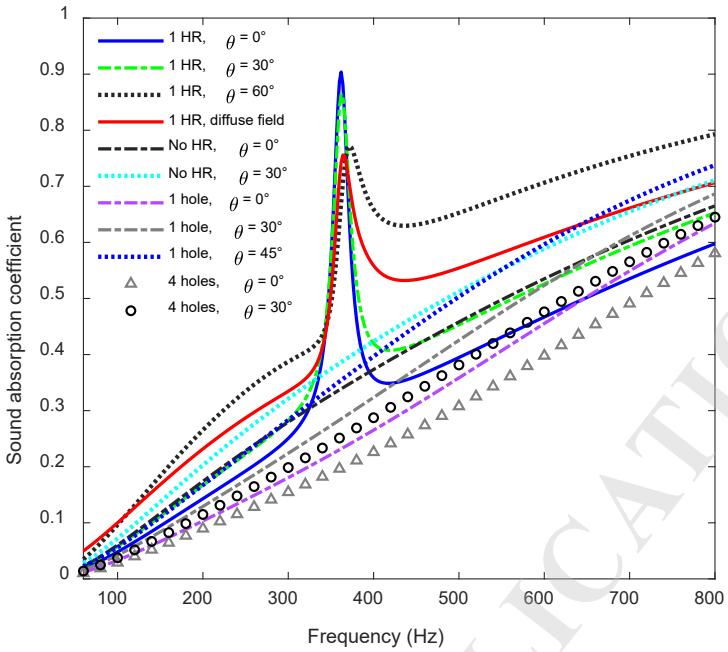

Fig. 12. Sound absorption coefficient of the metamaterial.

Figure 13 shows the oblique incidence and the diffuse field sound absorption coefficient of the porous material with four different incorporated resonators as illustrates in Fig. 1(b). As θ increases up to 40°, the sound absorption coefficient with 4 HR shows 4 identical resonant frequencies of 408 Hz, 448 Hz, 490 Hz and 530 Hz. The sound absorption peaks at these 4 resonant frequencies are 0.98, 0.99, 0.976 and 0.92 respectively for $\theta = 0°$ while for $\theta = 40°$, they are 0.985, 0.99, 0.94 and 0.84. The diffuse field sound absorption with 4 HRs presents four resonant peaks of 0.95, 0.94, 0.87 and 0.76 respectively at the resonant frequencies, while without HR, the values of the absorption coefficient at the resonant frequencies are 0.5, 0.53, 0.57 and 0.6 respectively. Above 70°, the absorption coefficient is lower as the incidence angle increases. Indeed, for an incidence angle of 88°, the absorption coefficient without HR is lower than 0.2 and presents 4 peaks of 0.28, 0.3, 0.32 and 0.4 with 4 HRs.

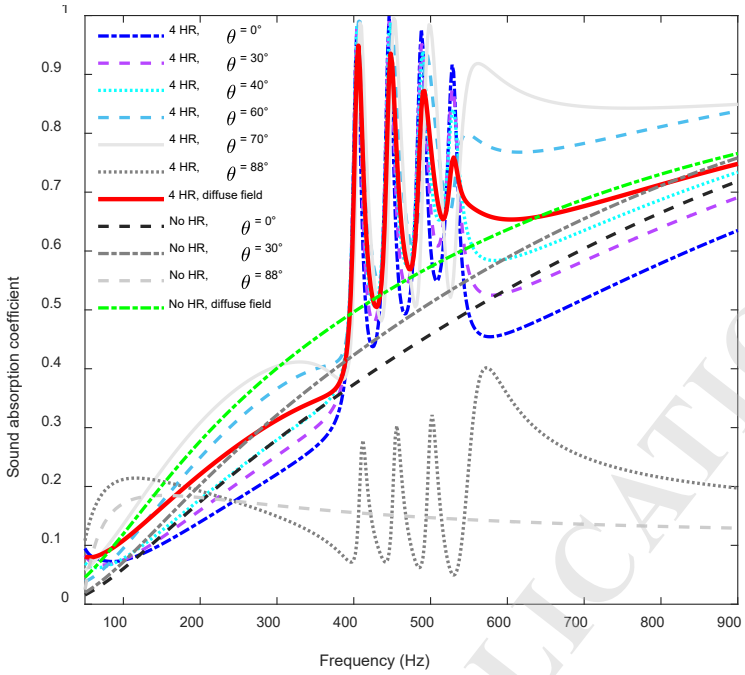

Fig. 13. Diffuse field sound absorption of the metamaterial with four embedded resonators.

The sound absorption coefficient at various incidence angles as well as the diffuse field absorption coefficient of the metamaterial in Fig. 1(c) made of porous material with 9 embedded resonators are shown in Fig. 14 and compared to the sound absorption without the resonators. The corresponding normal incidence TL is presented in Fig. 15 as well as the TL of the porous layer alone and that of the porous layer with nine perforations. When θ increases up to 50°, the absorption coefficient in Fig. 14 with 9 HRs presents nine resonant frequencies around 408 Hz, 448 Hz, 490 Hz, 530 Hz, 572 Hz, 612 Hz, 654 Hz, 694 Hz and 734 Hz. The absorption peak values for normal incidence in Fig. 14 are 0.82, 0.9, 0.94, 0.98, 0.98, 0.99, 0.984, 0.98, and 0.95 while the diffuse field absorption peak values are 0.87, 0.9, 0.93, 0.94, 0.95, 0.96, 0.91, 0.9 and 0.87 respectively. Without the embedded resonators, the diffuse field absorption coefficient increases from 0.47 at 370 Hz to 0.73 at 800 Hz. The absorption coefficient is significantly improved at the 9 resonant frequencies of the nine resonators. The TL of the metamaterial with 9 HR in Fig. 15 exhibits nine resonance peaks of 12.9 dB, 14.4 dB, 14 dB, 15.7 dB, 18 dB, 15.7 dB, 16 dB 16.5 dB and 13 dB at the resonance frequencies and outside these frequencies the TL is about 9 dB while without the resonators, the TL is between 7 and 8 dB. The TL of the porous layer with nine perforations is lower than 5 dB over the entire frequency range. The diffuse field sound absorption and the TL in Figs. 14 and 15 are significantly enhanced at the resonance frequencies of the

resonators. Compared to Fig. 13, it can be observed that the frequency band of the absorption coefficient increases as the number of resonators within the unit cell increases.

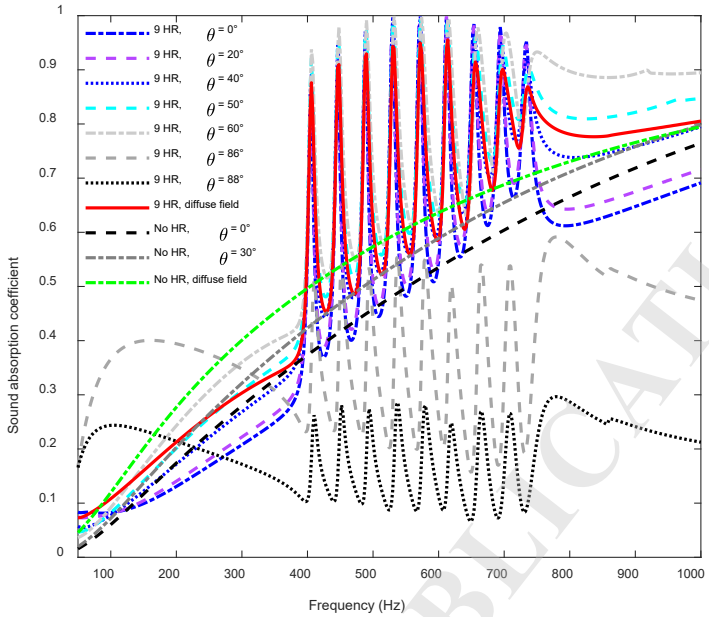

Fig. 14. Diffuse field sound absorption of the metamaterial with nine embedded resonators.

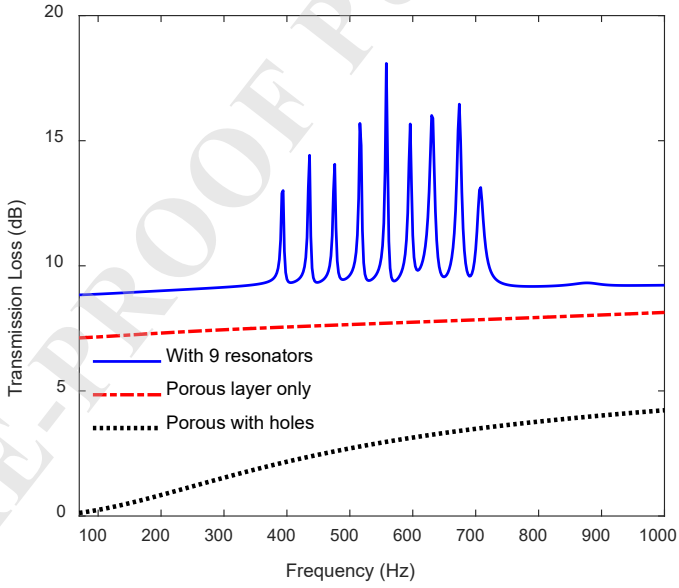

Fig. 15. Transmission loss of the metamaterial with nine embedded resonators.

Figure 16 shows the absorption coefficient at different incidence angles and the diffuse field sound absorption of the porous material with sixteen different embedded resonators as illustrated in Fig. 1(d). With sixteen embedded resonators, the absorption coefficient for each incidence angle shows sixteen resonance peaks in Fig. 16 with the peak values that are between 0.54 and 0.95. The

frequency band of the sound absorption in Fig. 16 is larger than the one in Fig. 14 for the porous layer with nine embedded resonators. The absorption coefficient decreases mainly when the incidence angle is higher than 75°.

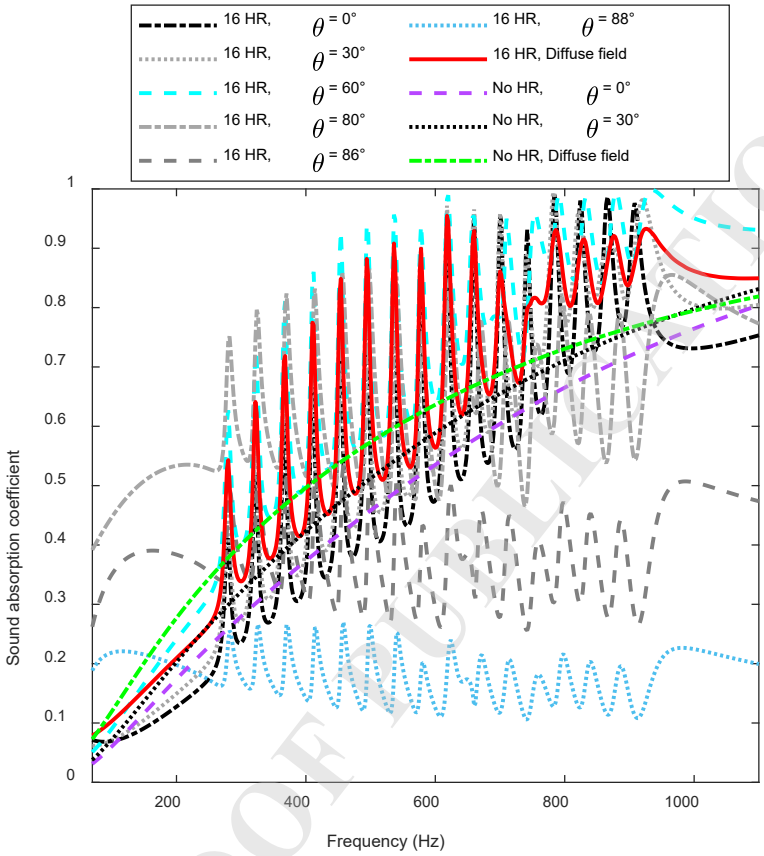

Fig. 16. Diffuse field sound absorption of the metamaterial with sixteen embedded resonators.

The sound attenuation mechanism of the metamaterial is investigated in the following. One considers the material design of Fig. 1(b) where the PUC is made of 4 parallel resonators that are incorporated into the porous layer. The sound absorption coefficient in Fig. 13 showed four resonant peaks at 408 Hz, 448 Hz, 490 Hz and 530 Hz and when the incidence angle is greater than 70°, the absorption coefficient decreases. Figure 17 illustrates the total root mean square (RMS) acoustic pressure through the metamaterial at 300 Hz, 408 Hz, 448 Hz, 490 Hz, 530 Hz and 700 Hz for incidence angle of 0° and 75°. The total acoustic velocity at the four resonant frequencies are shown in Fig. 18 while Fig. 19 presents the acoustic power dissipation density.

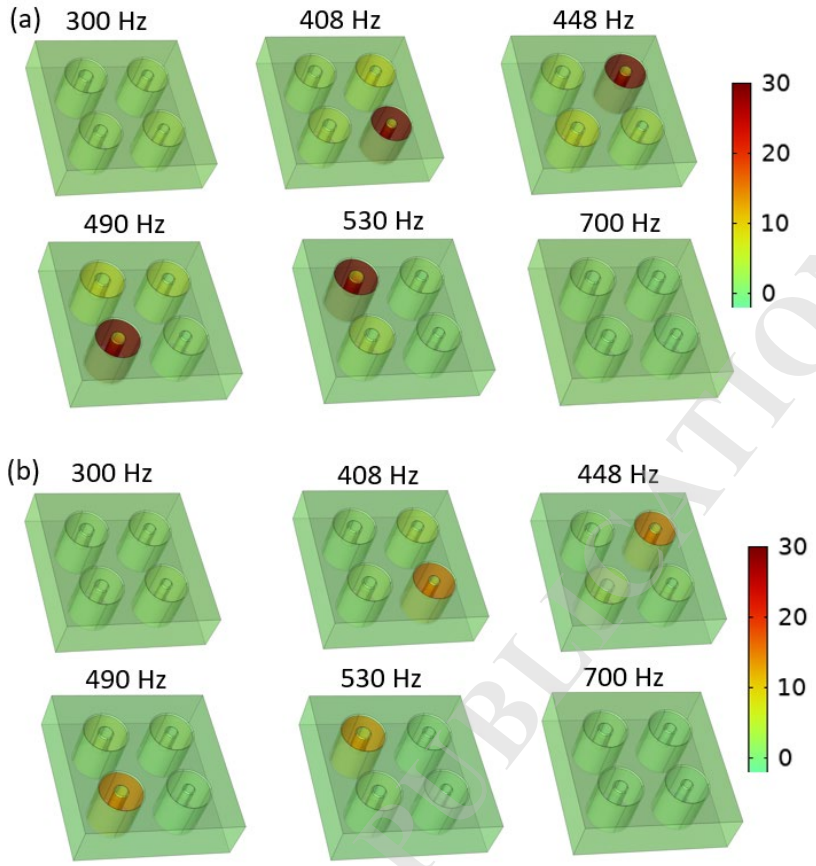

Fig. 17. Total RMS acoustic pressure (Pa) (a) θ = 0°, (b) θ = 75°.

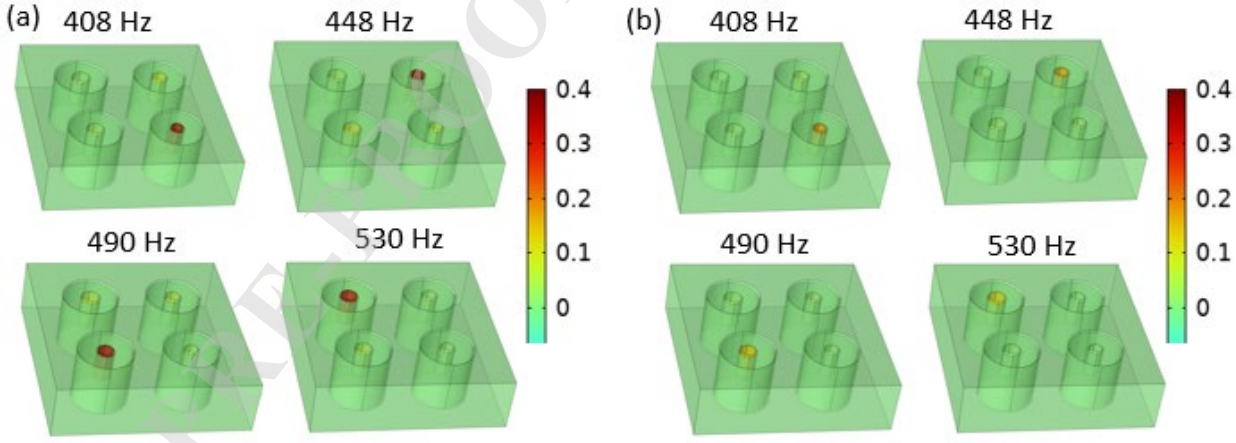

Fig. 18. Total acoustic velocity (m/s) (a) θ = 0°, (b) θ = 75°.

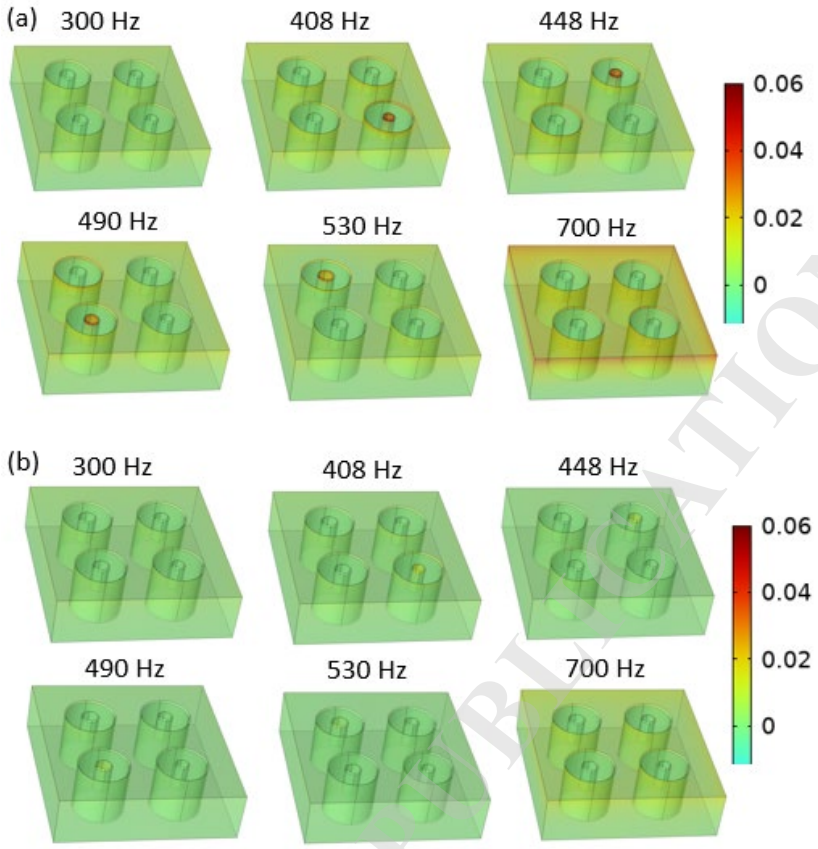

Fig. 19. Acoustic power dissipation density (W/m^3) (a) $\theta = 0°$, (b) $\theta = 75°$.

For a normal incidence, it is observed in Fig. 17(a) that the RMS acoustic pressure at each resonance frequency is maximum in the cavity of the corresponding resonator and reaches 30 Pa. Outside these resonance frequencies the acoustic pressure is very low in the cavities. The acoustic velocity in Fig. 18 is maximum reaching 0.4 m/s in the neck of each resonator at the corresponding resonance frequency and the acoustic power dissipation density is significant in the neck at the resonance frequency. As the frequency increases above the highest resonance frequency associated with HRs, the power dissipation density in the porous layer becomes most significant and sound absorption is mainly due to the porous material matrix. The 4 parallel resonators act independently resulting in 4 absorption peaks. For an incidence angle of 75°, the acoustic pressure in the cavities at the resonance frequencies decreases, the acoustic velocity in the necks (Fig. 18(b)) becomes low and the power dissipation density is negligible in Fig. 19(b) and consequently the absorption coefficient becomes low as observed in Fig. 13.

6. Conclusion

A design of acoustic metamaterial made of porous material with multiple embedded Helmholtz resonators was proposed and studied for multi-tonal and broadband noise reduction. A theoretical approach based on transfer matrix method was presented and the theoretical results of the sound absorption and the transmission loss showed good agreement with FEM. Compared to the porous layer with one embedded Helmholtz resonator that presents one resonant peak, the metamaterial consisting of the porous material with four, nine, and sixteen embedded Helmholtz resonators exhibits respectively four, nine and sixteen sound absorption and TL resonant peaks. The impacts of the incidence angles were demonstrated and the diffuse field sound absorption was significantly improved at the resonant frequencies of the resonators. The TL and sound absorption frequency band increases as the number of resonators within the porous layer increases. The proposed metamaterial can help in multiple engineering applications for multi-tonal and broadband noise attenuation.

References

Abbad, A. *et al.* (2019) "Numerical and experimental investigations on the acoustic performances of membraned Helmholtz resonators embedded in a porous matrix," *Journal of Sound and Vibration*, 459, p. 114873. Available at: https://doi.org/10.1016/J.JSV.2019.114873.

Allard, J.F. and Atalla, N. (2009) "Propagation of Sound in Porous Media: Modelling Sound Absorbing Materials," *Propagation of Sound in Porous Media: Modelling Sound Absorbing Materials*, pp. 1–358. Available at: https://doi.org/10.1002/9780470747339.

Boutin, C. and Becot, F.X. (2015) "Theory and experiments on poro-acoustics with inner resonators," *Wave Motion*, 54, pp. 76–99. Available at: https://doi.org/10.1016/J.WAVEMOTI.2014.11.013.

Doutres, O., Atalla, N. and Osman, H. (2015) "Transfer matrix modeling and experimental validation of cellular porous material with resonant inclusions," *The Journal of the Acoustical Society of America*, 137(6), pp. 3502–3513. Available at: https://doi.org/10.1121/1.4921027.

Ghinet, S., Bouche, P., Padois, T., Pires, L., Doutres, O., Kone, C. T., Triki, K., Abdelkader, F., Panneton, R. & Atalla, N. Experimental validation of acoustic metamaterials noise attenuation performance for aircraft cabin applications, In Proceedings of 2020 Inter-national Congress on Noise Control Engineering, INTER-NOISE 2020, 23-26 August 2020 Seoul, South Korea.

Kone, T.C. *et al.* (2021) "Optimization of metamaterials with complex neck shapes for aircraft cabin noise improvement," *Proceedings of INTER-NOISE 2021 - 2021 International Congress and Exposition of Noise Control Engineering* [Preprint]. Available at: https://doi.org/10.3397/IN-2021-2567.

Kone, T.C. *et al.* (2022) "Control and broadening of multiple noise frequencies using an assembly of sub-metamaterials connected by membranes for aircraft noise mitigation.," *Internoise 2022 - 51st International Congress and Exposition on Noise Control Engineering* [Preprint]. Available at: https://doi.org/10.3397/IN_2022_0663.

Lagarrigue, C. *et al.* (2013) “Absorption of sound by porous layers with embedded periodic arrays of resonant inclusions,” *The Journal of the Acoustical Society of America*, 134(6). Available at: https://doi.org/10.1121/1.4824843.

Laly, Z. *et al.* (2023) “Design and analysis of periodic acoustic metamaterial sound insulator using finite element method,” *Noise Control Engineering Journal*, 71(5), pp. 344–364. Available at: https://doi.org/10.3397/1/377128.

Laly, Z., Mechefske, C., Ghinet, S. and Kone, C.T. (2024) “Finite element modeling of acoustic metamaterial based on periodic Helmholtz resonator with a membrane in the cavity,” *Noise Control Engineering Journal*, 72(6), pp. 514–542. Available at: https://doi.org/10.3397/1/377239.

Laly, Z., Mechefske, C., Ghinet, S., Kone, C.T., *et al.* (2024) “The effects of Helmholtz resonator wall elasticity on the sound attenuation performance,” *Noise Control Engineering Journal*, 72(6), pp. 543–563. Available at: https://doi.org/10.3397/1/377240.

LALY, Z. *et al.* (2025) “Diffuse field sound absorption performance of porous material with embedded periodic Helmholtz resonators,” *INTER-NOISE and NOISE-CON Congress and Conference Proceedings*, 272(3). Available at: https://doi.org/10.3397/in_2025_1074286.

Laly, Z., Panneton, R. and Atalla, N. (2022) “Characterization and development of periodic acoustic metamaterials using a transfer matrix approach,” *Applied Acoustics*, 185, p. 108381. Available at: https://doi.org/10.1016/J.APACOUST.2021.108381.

Magliacano, D. *et al.* (2024) “Sound transmission properties of a porous meta-material with periodically embedded Helmholtz resonators,” *Mechanics of Advanced Materials and Structures*, 31(25), pp. 6748–6756. Available at: https://doi.org/10.1080/15376494.2023.2237699.

Verdière, K. *et al.* (2013) “Transfer matrix method applied to the parallel assembly of sound absorbing materials,” *The Journal of the Acoustical Society of America*, 134(6), pp. 4648–4658. Available at: https://doi.org/10.1121/1.4824839.

Zhang, W. and Xin, F. (2024) “Broadband low-frequency sound absorption via Helmholtz resonators with porous material lining,” *Journal of Sound and Vibration*, 578, p. 118330. Available at: https://doi.org/10.1016/J.JSV.2024.118330.

Zhu, X.F. *et al.* (2019) “Broadband low-frequency sound absorption by periodic metamaterial resonators embedded in a porous layer,” *Journal of Sound and Vibration*, 461, p. 114922. Available at: https://doi.org/10.1016/J.JSV.2019.114922.